Author for correspondence:
J. Parmentier
e-mail: jparmentier@uliege.be

A drop does not fall in a straight line: a rationale for the width of stalagmites

J. Parmentier[1], S. Lejeune[1], M. Maréchal[2], F. Bourges[3], D. Genty[4], V. Terrapon[1], J.-C. Maréchal[5] and T. Gilet[1]

[1]Department of Aerospace and Mechanics, University of Liège, Liège, Belgium
[2]University of Montpellier, Montpellier, France
[3]Géologie-Environnement-Conseil, Saint-Girons, France
[4]Environnements et Paléoenvironnements Océaniques et Continentaux, University of Bordeaux, Bordeaux, France
[5]Bureau de Recherches Géologiques et Minières, University of Montpellier, Montpellier, France

JP, 0000-0001-8263-8371; JCM, 0000-0001-8179-1294;
TG, 0000-0002-7339-7796

Drops loaded in calcium ions detach from stalactites and impact the underlying stalagmites, thereby allowing these latter to grow through calcite precipitation. Nevertheless, little is known about the influence of the drop free fall and splash dynamics on stalagmite shape and width. Through high-speed imaging of impacting drops on stalagmites from several caves, we observed that the impact point position of the drops is scattered, sometimes over several centimetres. We show that this dispersal has no external cause and must, therefore, be self-induced. Using a Langevin-like equation, we then propose a prediction of the impact point dispersal as a function of the falling height travelled by the drops. We finally show that measured stalagmite widths are correlated to the dispersal in the impact point position of the drop.

1. Introduction

Stalagmites are formed through the precipitation and deposition of calcite ($CaCO_3$) within the thin water film that covers their summit. Their vertical growth rate varies between 10 and 1000 $\mu m\,y^{-1}$ [1], as inferred by measuring e.g. the size of the annual laminae seen in vertical cross sections of stalagmites. Each

drop falling from the above stalactite and impacting this film brings new calcium and bicarbonate ions. The stalagmite growth rate depends on the concentration of these ions [2], which is set by the dissolution of limestone upstream [3]. The calcium ions precipitate in the film as long as the partial pressure p_{CO_2} of the cave is sufficiently low [4–6].

The growth rate also depends on the dripping rate at which the water within the film is partially renewed. This rate varies with both inter-annual and seasonal changes of recharge and weather events [7,8]. Dripping rates are higher during the rainy season [9], at least when the groundwater path upstream of the stalactite is sufficiently short [10]. Finally, the stalagmite growth rate depends on the thickness δ of the liquid film, which typically ranges between 50 and 300 μm. It likely results from a balance of the incoming flow rate that drips from the associated stalactite [11] and the gravity-induced drainage along the sides of the stalagmite, although there is currently no dedicated hydrodynamic model that rationalizes this assumption [12]. By contrast, a model that couples equations of chemical kinetics and thin-film hydrodynamics has already been proposed to describe the growth and shape of stalactites [13,14].

Since stalagmite growth is influenced by the incoming flow rate and the environmental parameters, stalagmites are often used as terrestrial paleoclimate proxies [15–17], especially in low- to mid-latitude regions where glacial ice cores or other continental proxies cannot be found [1]. Age-depth models [18] and duration of significant climate events such as severe droughts can be inferred, among others, from the annual laminae thickness [1]. Stalagmite laminae can even reflect overlying soil conditions and local hydrology when complementary records of cave external (climate, hydrology) and internal (evaporation, degassing) processes are available [19].

A complete model of the dissolution/precipitation kinetics of calcite coupled to the ion transport by molecular diffusion within a thin water film was proposed and validated experimentally by Buhmann & Dreybrodt [20,21]. These authors then suggested a numerical model [3,6] to estimate the vertical, time-averaged, growth rate of a stalagmite. The model was validated with growth rate measurements over several months [12,22,23]. It was also compared to ice and deep-sea core data by Kaufmann [24], who used temperature variations along with changes in precipitation and soil coverage to derive stalagmite stratigraphies reflecting paleoclimate variations over long periods of time (greater than 300 000 years). Although Dreybrodt's model yields a good approximation of the average vertical growth rate (though once the film thickness is arbitrarily adjusted), it fails at capturing the horizontal heterogeneity of the lamina thickness, caused e.g. by stalagmite roughness and curvature [12]. Therefore, it cannot reproduce the wide variety of stalagmite shapes and sizes observed in a cave (e.g. the flat top stalagmite of figure 1a–e versus the splash-cup stalagmite of figure 1f). Consequently, only cylindrical, 'candlestick' stalagmites were used so far as paleoclimate proxies because of their apparent regularity [1].

Dreybrodt's model mainly lacks a characterization of the dynamics of both the impacting drop and the water film. For instance, drops are assumed to always land at the apex of the stalagmite [12,25,26]. In this paper, we demonstrate that this hypothesis is not verified on most stalagmites. We investigate how the fluid dynamics of falling and splashing drops could set some constraints on stalagmite shape and width.

We report high-speed imaging measurements of radius, speed and impact position of drops falling on stalagmites in several different caves, as well as in a more controlled laboratory setting. We then show that these measurements are correlated to the height of fall and we propose a theoretical model to rationalize this fact. We also study the spreading of the liquid drop upon impact. Finally, we show that the stalagmite width can be predicted from the calculated impact point dispersal.

2. Results and discussion

(a) Phenomenology

Figure 1 depicts the impact of a drop on the flat top of a stalagmite at different times. The incoming drop (figure 1a) of radius $R \simeq 2.61$ mm is slightly flattened. It impacts the stalagmite at speed
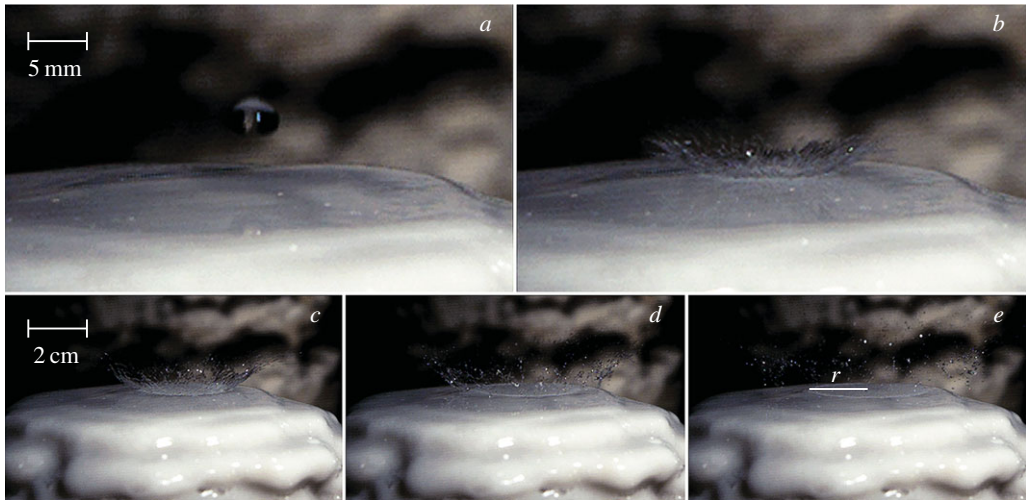
Figure 1. (*a*–*e*) Time sequence of the impact of a drop on stalagmite Org02 (Salle de Joly, Orgnac cave), with lamella spreading and crown formation. All frames (*a*–*e*) are separated by 1.3 ms. (*a*) The drop of radius 2.61 mm at most 600 μs before the impact. (*b*) Formation of the crown at least 600 μs after the drop crushed on the stalagmite. (*c*) Spreading of the lamella in the water residual film and ejection of secondary droplets. (*d*) Fragmentation of the crown. (*e*) The lamella has reached the stationary value $r = 2.1$ cm, around 5 ms after the initial impact. (Online version in colour.)
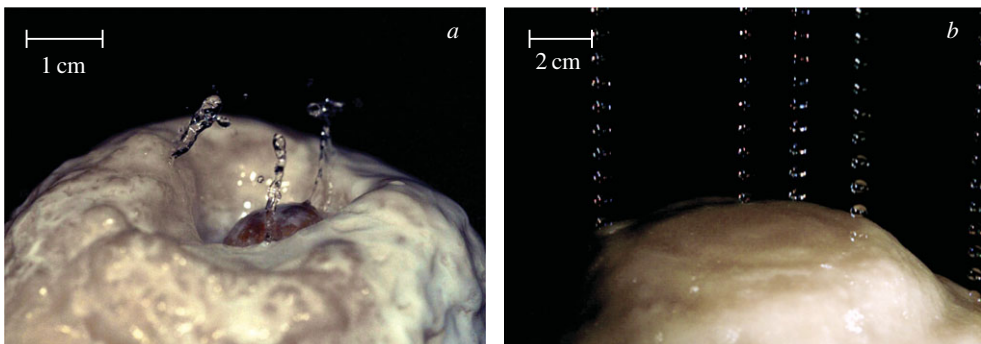
Figure 2. (*a*) Drop impact in a splash-cup stalagmite (Org07), with a small pisolite inside. Picture was taken 15 ms after the initial impact. (*b*) Drops coming from the same stalactite fall in different locations on the stalagmite Sal01, from La Salamandre cave. This image was obtained by superimposing frames showing the trajectories followed by five drops landing on this stalagmite. For each drop, the frames used are all separated by 740 μs, from the moment the drop appears in the field of view, up to right before impact. With a falling height of $z_0 = 25.6$ m, the value of Δ obtained for this stalagmite is 3.75 cm while its top radius s_t equals 5.50 cm. (Online version in colour.)

$v_0 \simeq 9.39$ m s^{-1}. The impact is accompanied by the formation of a liquid lamella surrounded by a crown (figure 1*b,c*). Secondary droplets are ejected from the edge of the growing crown (figure 1*c*). The crown then fragments into many droplets (figure 1*d*). Finally, the rim surrounding the liquid lamella reaches its maximal visible extension $r \simeq 2.10$ cm (figure 1*e*).

The drop impact on a concave stalagmite looks different. The lamella is deflected during its spreading by the curved stalagmite top. The liquid is ejected away in a few preferential directions constrained by the shape of the stalagmite (figure 2*a*).

It is also observed that drops in caves do not fall along vertical straight lines. Indeed, drops originating from a single punctiform stalactite impact the underlying stalagmite at different

positions, sometimes scattered over several centimetres. Figure 2*b* shows five drops coming from one stalactite but landing on different spots on the same stalagmite, up to 13.15 cm apart.

(b) Dripping

Drop radius R was measured in caves for all drops impacting the stalagmites summarized in table 2. These measurements suggest that R is fairly constant, with a value for all drops of 2.63 ± 0.18 mm (mean $\pm$ s.d.).

These observations can be rationalized as follows. When water reaches the tip of the stalactite, it forms a growing pendant drop. Once the drop becomes sufficiently heavy, surface tension can no longer hold it still, and the drop falls [27]. The weight of the pending drop is $4/3\pi R^3 \rho g$, where R is the drop radius, $\rho \simeq 1000 \, \text{kg m}^{-3}$ is the water density and g the acceleration of gravity. The maximum drop weight that can be balanced by surface tension forces is of the order of $2\pi \sigma r_{st}$, where $\sigma \simeq 70 \, \text{mN m}^{-1}$ is the surface tension of water and r_{st} is the stalactite outer radius. Because the stalactite is formed by the drop itself, the tip radius of the stalactite should approximately match the drop equivalent radius, i.e. $r_{st} = cR$, where c is a proportionality constant. With $c = 2/3$ of the order of unity, the drop radius R would be estimated as $\sqrt{3c\sigma/2\rho g} \simeq 2.6$ mm, as measured. The parameters involved can be considered as constant in the temperature and pressure range encountered in caves, hence R is also fairly constant from one stalactite to another and in between different drops falling from a given stalactite [28] (electronic supplementary material, figure S6).

The size of a dripping drop R slightly depends on the water flow rate feeding the stalactite [9]. This flow rate is inversely proportional to the dripping period t_0 separating two successive dripping events from the same stalactite, which is observed to vary seasonally from less than a second to several months, $t_0 \in [10^{-1}, 10^7]$ s. When $t_0 \lesssim 1$ s, the drop volume decreases and satellite droplets form [9]. Nevertheless, the drop formation from stalactites always remains in the periodic dripping regime (contrary to jetting or chaotic dripping) since the capillary time of the drop $\sqrt{\rho R^3/\sigma} \simeq 50$ ms is always smaller than t_0 [29].

(c) Free fall and impact point dispersal

In figure 3, the impact velocity v_0 of drops is represented as a function of their falling height z_0. Data obtained in caves and in a laboratory setting are in good agreement with each other. The velocity v_0 increases nonlinearly with the falling height z_0. It seems to reach a saturation value for large falling heights ($z_0 > 20$ m).

The horizontal position of drop impacts, measured in one vertical plane, approximately follows a Gaussian distribution. Since both the drop and the stalactite from which it originates are relatively axisymmetric, we may assume that the two-dimensional distribution of horizontal impact positions is also axisymmetric. Figure 4 shows the measured standard deviation Δ of this impact position distribution as a function of the falling height z_0. The impact point dispersal Δ increases almost linearly with z_0.

Again, data obtained in caves and more controlled laboratory conditions overlap. Therefore, the scatter of impact position cannot be attributed to a factor specific to caves. For example, while the small irregularities at the surface of the stalactite might give the drop some initial horizontal momentum when this latter detaches, such momentum would be systematic and would not lead to a Gaussian dispersal. The local wind originating from the venting of the cave might also induce some additional drift to the drop. However, such contribution seems negligible. For example, a maximal airflow rate of the order of $160\,000 \, \text{m}^3 \, \text{d}^{-1}$ was measured at the open-air entrance of the first room (salle de Joly) of Orgnac's cave [30]. Because the cave cross section is about $2500 \, \text{m}^2$, the background air speed should be of $0.7 \, \text{mm s}^{-1}$. A drop falling at more than $8 \, \text{m s}^{-1}$ takes less than 4 s to achieve a 30-m fall and would only be deviated at most by 3 mm. Hence, background air currents cannot explain the scattering of the drop impact point in our data. Moreover, the same distribution is observed in the laboratory, although the drop fall is protected from parasitic air currents. The apparently random deviation in drop trajectory must, therefore, be self-induced.
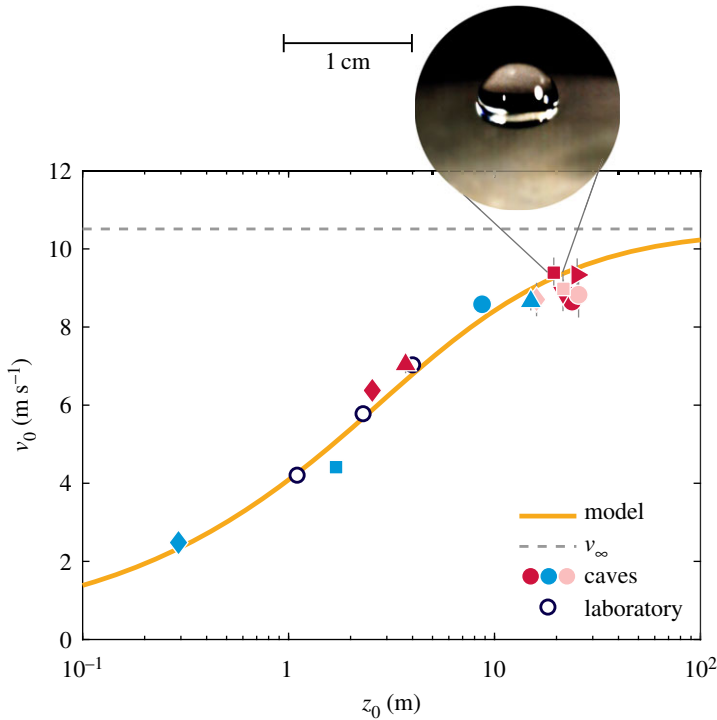
Figure 3. Impact velocity v_0 of the drop as a function of falling height z_0 measured in both cave and laboratory settings (symbols), compared to the prediction given by equation (2.6) (solid line in yellow) for parameters $c_1 = 0.198$ and $c_2 = 0.029$, with a drop radius $R = 2.64$ mm. The dashed line shows the terminal velocity $v_\infty = 10.5$ m s^{-1} that drops could reach based on these experimental data. Hollow symbols circle represents laboratory data corresponding to a drop radius $R = 2.32$ mm similar to that encountered in caves. Solid symbols in red (dark grey in printed version), pink (light grey in printed version) and blue (medium grey in printed version) represent cave data, one per stalagmite from table 2 for which high-speed videos were taken (cf. table 2; electronic supplementary material, table S1, for symbols correspondence). The inset of the graph shows a picture of a drop flattened because of air friction, at most 600 µs before its impact on Org02 (Salle de Joly, Orgnac cave). The equivalent radius of this drop $R = 2.61$ mm, its falling height $z_0 = 19.40$ m and the impact velocity $v_0 = 9.39$ m s^{-1}. (Online version in colour.)

We will attempt to model the influence of aerodynamic forces on the trajectory of the falling drop through a Langevin equation. The drop position is denoted $\mathbf{X} = \mathbf{x} + z\,\mathbf{e}_z$, where $\mathbf{x} = (x, y)$ is horizontal and $\mathbf{e}_z$ is a vertical unit vector oriented upwards. The velocity and acceleration of the drop are given by $\dot{\mathbf{X}} = \dot{\mathbf{x}} + v\,\mathbf{e}_z$ and $\ddot{\mathbf{X}} = \ddot{\mathbf{x}} + \dot{v}\,\mathbf{e}_z$, respectively.

The motion of a falling drop of mass $M = 4/3\pi\rho R^3$ satisfies Newton's second law

$$M\ddot{\mathbf{X}} = -Mg\,\mathbf{e}_z + \mathbf{F}, \tag{2.1}$$

where Mg is the weight and $\mathbf{F}$ is the aerodynamic force. This latter comprises the drag, opposed to the drop motion, and an additional lift component in a plane perpendicular to the drop motion

$$\mathbf{F} = -C_D \frac{\rho_a S |\dot{\mathbf{X}}|}{2} \dot{\mathbf{X}} - C_L \frac{\rho_a S |\dot{\mathbf{X}}|}{2} \mathbf{e}_r \times \dot{\mathbf{X}}, \tag{2.2}$$

where $\rho_a \simeq 1.2$ kg m^{-3} is the air density, S is the cross-sectional area of the drop perpendicular to its motion, $\mathbf{e}_r$ is a unit vector of random direction in the plane perpendicular to $\dot{\mathbf{X}}$ and C_D and C_L are the drag and lift coefficients, respectively. The lift appearing in the former equation is caused by the loss of symmetry in the wake of the falling drop, as explained in more detail in §2c(ii).

6

royalsocietypublishing.org/journal/rspa Proc. R. Soc. A **475**: 20190556
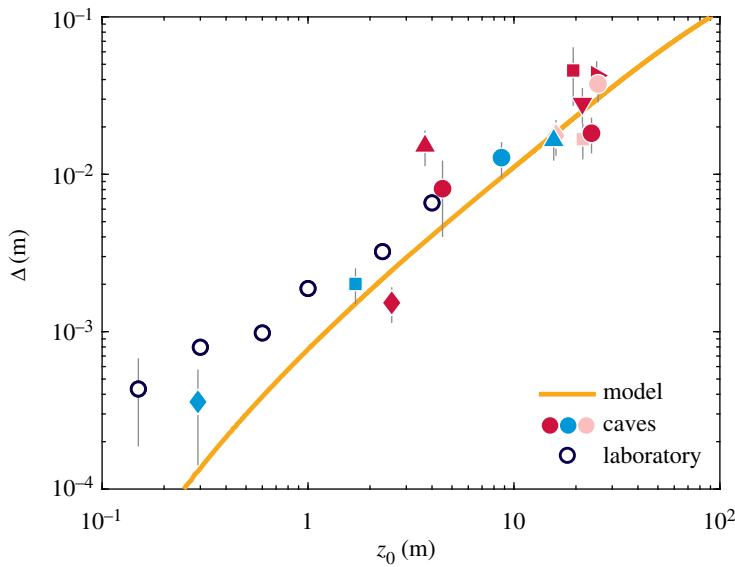
Figure 4. Standard deviation Δ of impact point position as a function of the falling height z_0. The yellow solid curve is obtained by solving numerically the recurrence relations from equations (2.10) and (2.11) and varying parameters v, f, Re, St and C_D at each vortex emission. The lift coefficient C_L is set to 0.067, as an average across Reynolds of the RMS values found in the literature (table 1). Hollow symbols circle correspond to data obtained in a laboratory setting for drops of radius $R = 2.32$ mm. All the solid symbols in red (dark grey in printed version), pink (light grey in printed version) and blue (medium grey in printed version) represent experimental measurements obtained in caves with high-speed videos (cf. table 2; electronic supplementary material, table S1, for symbols correspondence). (Online version in colour).

(i) Drop velocity

Since the drop is axisymmetric (axis $\mathbf{e}_z$) and its motion is mostly vertical ($C_L \ll C_D$), we expect both $|\dot{\mathbf{x}}| \ll v \Rightarrow |\dot{\mathbf{X}}| \simeq v$ and $(\mathbf{e}_z \times \mathbf{e}_r) \cdot \dot{\mathbf{X}} \ll \mathbf{e}_z \cdot \dot{\mathbf{X}}$. Consequently, the vertical component of the lift is negligible in comparison to the vertical component of the drag, and the vertical projection of equations (2.1) and (2.2) becomes

$$\dot{v} = g - \frac{C_D \rho_a S v^2}{2M}. \tag{2.3}$$

The drag coefficient C_D depends on the Reynolds number $\mathrm{Re} = 2R v \rho_a / \mu_a$, where $\mu_a \simeq 18 \times 10^{-6}$ Pa s is the dynamic viscosity of air. This dependence is here approximated in [31]

$$C_D = \begin{cases} \dfrac{24}{\mathrm{Re}}(1 + c_1 \mathrm{Re}^{2/3}) & \text{for } \mathrm{Re} < \mathrm{Re}_c, \\[2mm] \dfrac{24}{\mathrm{Re}_c}(1 + c_1 \mathrm{Re}_c^{2/3}) & \text{for } \mathrm{Re} \geq \mathrm{Re}_c, \end{cases} \tag{2.4}$$

which is valid for at least $\mathrm{Re} < 10^5$. For a hard sphere, $\mathrm{Re}_c \simeq 1000$ and $c_1 \simeq 0.175$, so $C_D \simeq 0.45$ when $\mathrm{Re} > \mathrm{Re}_c$. However, the drops are flattened in response to aerodynamic forces (inset of figure 3). Their deformation is resisted by surface tension, so dimensional analysis [32] would suggest that the effective, horizontal surface S is

$$S = \pi R^2 + 2\pi c_2 \frac{\rho_a R^3 v^2}{\sigma}, \tag{2.5}$$

with c_2 to be determined. Moreover, as the drop is liquid, it might not satisfy the same no-slip condition as a hard sphere. However, since tangential stresses remain continuous at the water/air interface, the ratio of characteristic velocity in the water versus in the air should be of the order of the ratio between dynamic viscosity in the air versus in the water. Because water viscosity is

around a hundred times larger than that of air, recirculation velocities inside the drop should be of the order of a hundredth of the vertical translation velocity of the drop. Consequently, the no-slip condition should apply in first approximation and the falling drop should experience a drag force close to that of a hard sphere.

Time integration of equation (2.3) gives the relation between the falling height of the drop z_0 and its impacting velocity v_0:

$$z_0 = \int_0^{v_0} \frac{v \, dv}{g - \frac{C_D \rho_a S v^2}{2M}}. \tag{2.6}$$

This relation is compared to the corresponding experimental results in figure 3. A least-square fit on velocity data (both from caves and laboratory) gives $c_1 = 0.198$ and $c_2 = 0.029$. The terminal speed $v_\infty \simeq 10.5 \, \mathrm{m \, s^{-1}}$ is attained when

$$Mg = \tfrac{1}{2} C_{D,\infty} \rho_a S_\infty v_\infty^2, \tag{2.7}$$

where $C_{D,\infty}$ and S_∞ are obtained by substituting $v = v_\infty$ in equations (2.4) and (2.5), respectively. This terminal velocity, associated with the fairly constant size of cave drops, yields an upper bound on the Reynolds number of $\mathrm{Re} \sim 3500$, which is still within the range of validity of equation (2.4).

While the drag-induced deformation of the drop significantly affects its falling speed, it is not sufficiently large to induce some in-flight fragmentation as experienced for example by large raindrops [32]. Indeed, the criterion for such fragmentation is $\rho_a R v^2 / \sigma > 15$. Given the size constraint on drops originating from stalactites, satisfying this criterion would require the falling speed to reach $17 \, \mathrm{m \, s^{-1}}$, which is well beyond the terminal speed $v_\infty = 10.5 \, \mathrm{m \, s^{-1}}$.

(ii) Drop horizontal deflection

The motion of a falling sphere is more complex than one would expect. Vortices appear periodically in the downstream wake of the drop as soon as $\mathrm{Re} \simeq 212$ [33,34]. This condition is already reached about 1.3 cm below the dripping point. Each vortex generates an aerodynamic force on the drop, inducing slight deviations from a straight vertical trajectory. At first, these vortices randomly choose and develop around a longitudinal plane of symmetry containing the sphere centre. As the Reynolds number increases to 320, the wake becomes irregular but the planar symmetry is still conserved up to $\mathrm{Re} = 355$, corresponding to a distance $z = 3.80 \, \mathrm{cm}$. Beyond this value, the wake becomes fully three-dimensional and chaotic. The break of symmetry in the wake past the drop is thus responsible for the apparition of the lift in equation (2.2).

We will assume here that successive vortex emissions are separated by a time T. On average, this time decreases with increasing Reynolds number. There is currently no analytical model that relates the dimensionless shedding frequency $\mathrm{St} = 2R/(vT)$ (Strouhal number) to Re for falling spheres. However, experimental data [35] suggest that St increases with Re, typically during the first 5 m of fall, up to approximately 0.9. Then St decreases with increasing Re but, in the range covered in caves, remains larger than 0.5. The St(Re) experimental data of Achenbach *et al.* [35] are approximated by a cubic polynomial in the range $\mathrm{Re} < 3500$.

We also hypothesize that the vortices emitted from a falling drop do not interact with the trajectory of the next drop. This is most likely true if the dripping period t_0 between two drops is larger than the time t_v over which vortices fade away by viscous dissipation. This time might be estimated as $t_v \sim \rho_a R^2/(4\mu_a) \simeq 10^{-1} \, \mathrm{s}$. In the visited caves, the smallest dripping period was of the order of 2 s, while it was often larger than 10 s. Hence, in the present case, we may consider that the passage of a drop does not influence the trajectory of subsequent ones.

Table 1. Root mean square values of lift coefficients C_L^{rms} obtained by different authors at various Reynolds numbers.

authors	Re	C_L^{rms}
Bagchi 2003 [34]	107	0.091
Bagchi 2003 [34]	261	0.058
Johnson 1999 [36]	211–250	0–0.062
Bouchet 2006 [37]	212–330	0–0.068
Plouhmans 2002 [38]	300	0.060
Plouhmans 2002 [38]	500	0.058
Bagchi 2003 [34]	609	0.081
Plouhmans 2002 [38]	1000	0.167
Yun 2006 [39]	3700	0.006
Yun 2006 [39], Jones 2008 [40]	10 000	0.046, 0.033

The impact point dispersal Δ is estimated as a function of the falling height z_0, by considering the horizontal projection of Newton's second law of motion

$$M\ddot{\mathbf{x}} = -\tfrac{1}{2}C_D\rho_a S v \dot{\mathbf{x}} + \tfrac{1}{2}C_L\rho_a S v^2 \mathbf{e}, \tag{2.8}$$

where $\mathbf{e} = \mathbf{e}_r \times \mathbf{e}_z$ is a vector of random horizontal direction that is almost unitary since the drop velocity is almost vertical. We neglect the drop deformation, which is here a second-order term, so the cross-sectional area S is now approximated by πR^2. No exact relation between the lift coefficient C_L and the Reynolds number could be found in the literature over the entire range of Re values covered by the falling drop, i.e. up to Re ~ 3500. However, the instant lift coefficient has been computed from numerical simulations at peculiar Re by several authors, as reported in table 1. All coefficients presented in this table correspond to root mean square values computed over a time period during which at least a few tens of vortices were shed. The lift coefficient remains of constant order of magnitude (except at Re = 3700, where the shear layer separates laminarly from the sphere whereas turbulence occurs within this layer [41]). The average value of all the lift coefficients presented in table 1 is $C_L = 0.067$. Equation (2.8) can be made dimensionless by defining $\tau = t/T$, $x = \mathbf{x}/(vT)$ and $\dot{x} = \dot{\mathbf{x}}/v$:

$$\ddot{x} = -c_D\dot{x} + c_L \mathbf{e}, \tag{2.9}$$

where $c_D = (3\rho_a/4\rho)(C_D/\mathrm{St})$ and $c_L = (3\rho_a/4\rho)(C_L/\mathrm{St})$.

The horizontal position and velocity of the drop can be obtained by first integrating equation (2.9) over one period T between two successive shedding events. We will assume that the lift component of the aerodynamic force remains constant in magnitude and direction over this shedding period. The horizontal position x_n and velocity $\dot{x}_n$ after the nth shedding are therefore related to the position x_{n-1} and $\dot{x}_{n-1}$ through the following Langevin-like recurrence relations, where $\alpha = \exp(-c_D)$:

$$x_n = x_{n-1} + \frac{(1-\alpha)}{c_D}\dot{x}_{n-1} + \frac{c_L}{c_D^2}(\alpha - 1 + c_D)\mathbf{e}, \tag{2.10}$$

$$\dot{x}_n = \alpha\dot{x}_{n-1} + \frac{c_L}{c_D}(1-\alpha)\mathbf{e}. \tag{2.11}$$

The standard deviation of the horizontal position is by definition $\Delta = vT\sqrt{\langle \mathbf{x_n} \cdot \mathbf{x_n}\rangle}$, where $\langle \cdots \rangle$ denotes an ensemble average over many falling drops. It is calculated by multiplying and

averaging equations (2.10) and (2.11):

$$\langle x_n \cdot x_n \rangle = \langle x_{n-1} \cdot x_{n-1} \rangle + \frac{(1-\alpha)^2}{c_D^2} \langle \dot{x}_{n-1} \cdot \dot{x}_{n-1} \rangle + 2\frac{(1-\alpha)}{c_D} \langle x_{n-1} \cdot \dot{x}_{n-1} \rangle$$

$$+ \frac{c_L^2}{c_D^4}(\alpha - 1 + c_D)^2, \tag{2.12}$$

$$\langle \dot{x}_n \cdot \dot{x}_n \rangle = \alpha^2 \langle \dot{x}_{n-1} \cdot \dot{x}_{n-1} \rangle + \frac{c_L^2}{c_D^2}(1-\alpha)^2 \quad \text{and} \tag{2.13}$$

$$\langle x_n \cdot \dot{x}_n \rangle = \alpha \langle x_{n-1} \cdot \dot{x}_{n-1} \rangle + \frac{\alpha(1-\alpha)}{c_D} \langle \dot{x}_{n-1} \cdot \dot{x}_{n-1} \rangle + \frac{c_L^2}{c_D^3}(1-\alpha)(\alpha - 1 + c_D). \tag{2.14}$$

Since the lift direction e is assumed to be random and uncorrelated with the drop horizontal position and velocity, both $\langle x_n \cdot e \rangle$ and $\langle \dot{x}_n \cdot e \rangle$ vanish, and $\langle e \cdot e \rangle = 1$.

These coupled recurrence relations can be solved numerically from rest initial conditions to find Δ. We consider that the velocity $v(z)$ increases at each vortex emission n according to equation (2.6), and Re, St and C_D vary accordingly, which is why equations (2.12) to (2.14) cannot be integrated analytically. Nevertheless, an analytical solution at v constant is presented in the electronic supplementary material. Solving the recurrence relations with the C_L value of 0.067 yields the numerical solution $\Delta(z_0)$ shown in figure 4. The model captures very well the measurements $\Delta(z_0)$, without any fitting parameter.

(d) Impact and initial spreading

All the drops filmed with high-speed imaging splashed at impact (figure 1), in contrast with an assumption of previous models of stalagmite growth [12]. Therefore, during the impact the drop crushes to form a lamella surrounded by a rim that grows with time. The rim destabilizes quickly into a collection of secondary droplets which are ejected away. The maximum radius r reached by the lamella formed at impact was measured for all recorded stalagmites. It does not strongly vary from one stalagmite to another. Hence, it can be considered as constant: $r \simeq 1.83 \pm 0.28$ cm (mean $\pm$ s.d. on all measurements).

Two main dimensionless parameters govern the drop impact dynamics: the ratio δ/R between the film thickness and the drop radius, and the Weber number defined as We $= 2\rho R v_0^2 / \sigma \simeq 5000$ for $v_0 = 10$ m s^{-1}. Hence, inertia dominates surface tension in cave impacts, and the hydrophilic nature of stalagmites does not influence significantly the impact dynamics [42]. During the impact, the drop first crushes on a timescale $2R/v_0 \lesssim 1$ ms for $v_0 \gtrsim 5$ m s^{-1}, then it spreads outwards. A crown may form as a result of a kinematic discontinuity, which is referred to as a splash. The literature is not abundant when it comes to splash on thin liquid films for which $\delta/R \ll 1$ [43]. Typically in caves, $\delta/R \lesssim 0.04$, which is difficult to reproduce experimentally. Some experiments [44] for $\delta/R \in [0.05, 0.1]$ suggest that the threshold for splashing is independent of δ and would occur in caves when We > 400, which corresponds to a velocity $v_0 \simeq 2.3$ m s^{-1} and a falling height $z_0 \simeq 30$ cm. This explains why all the observed drops splashed at impact.

In our experiments, the radius of the lamella r varies from one stalagmite to another by at most 15% for impact velocities v_0 ranging in $[2.5, 10]$ m s^{-1} and film thickness δ ranging in $[40, 300]$ μm (electronic supplementary material, figures S2–S5). An ANOVA test was performed on data from 13 stalagmites to assess the possible influence of We and δ on the radius r. The p-values returned were 2.3×10^{-4} for We, and 0.1 for δ. With a significance level of 5%, the variations of r induced by δ can thus be neglected, whereas the variations of r due to We should be taken into account. However, the literature [42,45–47] suggests that r should not strongly vary with We. For example, the scaling law $r \simeq 2R$ We$^{1/4}$ from Clanet et al. [42] would give 16% of variation of r, which is of the same order of magnitude as what we observed. Therefore, in first approximation, considering r as a constant should not lead to major errors.
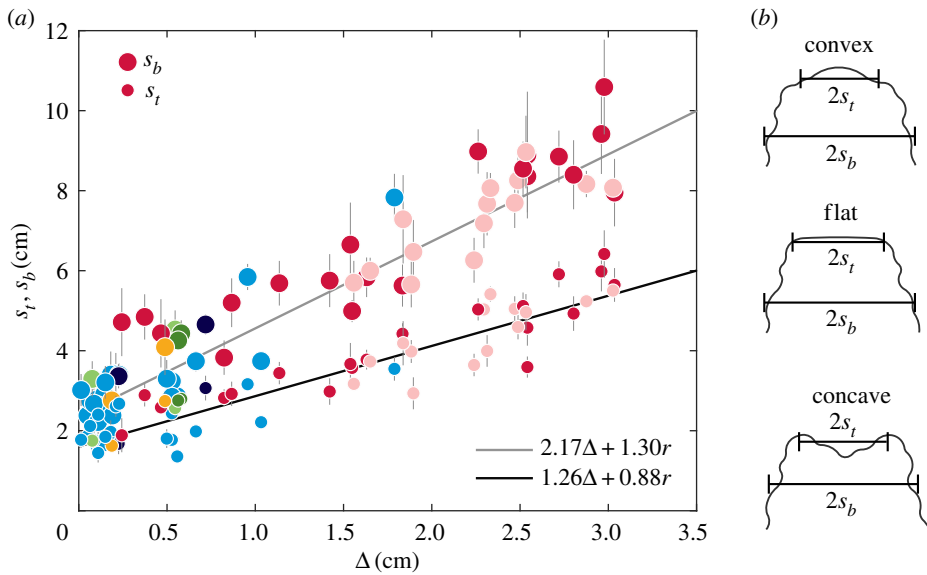
Figure 5. (a) Measured stalagmite top radius s_t (small symbols) and body radius s_b (large symbols) are shown as a function of the impact point dispersal Δ, computed from equations (2.12) to (2.14) from the measured falling height z_0 (electronic supplementary material, tables S1 and S2). Each symbol represents a single stalagmite, with one colour per cave (table 2). The black and grey solid lines correspond to equations (2.15) and (2.16), respectively. (b) Corresponding radii for each stalagmite type. (Online version in colour.)

(e) Stalagmite width

Two types of characteristic radii were measured for 65 candlestick stalagmites fed by single drips from seven different caves (cf. §4): the radius of the top plateau, s_t, and the radius of the stalagmite body s_b, taken as the average radius along the whole stalagmite. These two radii are represented in figure 5 with respect to the impact point dispersal $\Delta(z_0)$ computed from equations (2.12) to (2.14) and the measured falling height z_0 corresponding to each stalagmite. There is a significant correlation between the stalagmite radii, s_t and s_b, and Δ. A linear regression yields

$$s_t = 1.26\Delta + 0.88r \tag{2.15}$$

and

$$s_b = 2.17\Delta + 1.30r. \tag{2.16}$$

For very small falling heights there is almost no dispersion of the impact point, meaning that drops always fall at the centre of the stalagmite. The stalagmite width would therefore be mostly governed by the maximum size of the lamella formed at impact, r. The intercept of equation (2.15) with the axis $\Delta = 0$ (corresponding to no fall-induced dispersion) is indeed close to the average value obtained for r. Curl [11] already computed a minimum stalagmite radius of approximately 1.5 cm, close to r, by dividing the drop volume by the estimated film thickness. In equation (2.16), the slope of 1.30, larger than unity, may be due to the widening of the stalagmite owing to the gravity-driven drainage of the water film, which is not taken into account here.

As the falling height increases both radii s_t and s_b are expected to expand as well because of the growing impact point dispersal. In particular, for s_b, almost twice the standard deviation of the impact point distribution is added to the maximum spreading radius of the lamella. Since the distribution is Gaussian, the probability that a drop falls on such a surface is at least 90%.

A more comprehensive description of the width variations over the entire stalagmite would require to take the influence of additional parameters into account. A non-exhaustive list includes (i) the dripping period that varies in response to inter- and intraseasonal fluctuations in water

provision, (ii) the precipitation rate that varies with the water pH and temperature, and partial pressure in CO_2 in the cave, p_{CO_2}, and (iii) the gravity-induced drainage of the film over the stalagmite topography. The timescales corresponding to these phenomena should be compared as they are representative of competing processes governing stalagmite growth.

3. Conclusion

We proposed a new approach to rationalize stalagmite width by focusing on the fluid dynamics underlying their growth. The stalagmite width is not only governed by the saturation size of the spreading lamella r, but it is also and mostly conditioned by the dispersal of the drop impact position, Δ, as our measurements revealed.

   This impact point position dispersal Δ is due to the vortices emitted in the wake of the falling drop and increases almost linearly with the falling height z_0. Large stalagmites originating from a single stalactite are therefore found in cave parts with high ceilings. The radius r of spreading upon impact seems to depend weakly on the impact velocity v_0 of the drop and is found to be fairly constant in our experiments, as already suggested by several authors. We developed a model based on a Langevin equation that rationalizes our measurements of impact point dispersal without the need of any fitting parameter. This model would be applicable to the free fall of drops and similar objects in other contexts.

   While our measurements and model respectively show and explain the correlation between stalagmite width, impact point dispersal and falling height, the stalagmite width may also be significantly influenced by several other factors affecting its growth, including the dripping period, the precipitation rate and the film drainage.

4. Material and methods

(a) Still pictures

Still pictures of 65 stalagmites were taken in seven different caves from the South of France (cf. table 2). Falling height z_0 was measured for all individuals by laser telemetry. For large falling heights (up to 27 m), uncertainty on the measurements might reach 50 cm, owing to the very irregular ceiling, and the difficulty to point exactly on the emitting stalactite.

   Stalagmites encountered in caves do not all have the same shape. We classified them into three categories depending on the shape of their apex: convex stalagmites, flat or concave. They can be seen, respectively, in figure 1*a,f*, figure 4. Two different radii were defined and measured for all individuals: s_t and s_b. First, s_t is taken at the very top of the stalagmite, and an average is made on 10 to 15 measurements performed on the first few centimetres from the top. For convex stalagmites, s_t corresponds to the largest chord of the apex. For flat stalagmites, s_t is the radius of the highest plate and for concave ones, it corresponds to the diameter of the inner cavity (figure 5). The second radius, s_b, corresponds to an average of about 30 measurements at various positions over a distance of 15 to 50 cm from the top.

(b) Videos

A total of 582 high-speed movies (5400 fps) of drops impacting some stalagmites (cf. table 2) were recorded with a Phantom Miro110 camera, then analysed using image processing tools. Additional information available only for these stalagmites include drop size R and impact velocity v_0, lamella radius r and impact point dispersal Δ.

   A complementary set of free fall measurements (R, $v_0(z_0)$ and $\Delta(z_0)$) was performed in a laboratory setting that offers more controlled conditions. Water drops of 2.32 mm radius were pushed out of the tube thanks to a syringe pump (AL-1000, World Precision Instruments) at a flow rate of 200 µl min^{-1}. The release height was varied between 15 and 400 cm, which determined the impact speed on the substrate. To prevent any parasitic air currents that could interfere with the

Table 2. Cave names and related colours. The number of stalagmites for which still pictures were taken is indicated in the third column for each cave. Among them, the number of stalagmites for which about 40 high-speed drop impact movies were recorded is indicated in the last column (electronic supplementary material, tables S1 and S2, figures S6–S11).

colour	cave	pictures	Sm. filmed
●	Bétharram	2	—
●	Clamouse	19	4
●	Esparros	2	—
●	Gargas	2	—
●	Niaux	2	—
●	Orgnac	13	7
●	La Salamandre	11	3

drops, the splash column was isolated by a plastic tube of diameter equal to 20 cm, which was sufficient to neglect the aerodynamic interaction of the falling drop with the tube.

(c) Film thickness measurements

A paper towel of known surface area and mass was gently placed on the stalagmite top to locally collect the liquid from the residual film. Measuring the difference in mass before and after soaking the paper allowed then to estimate the thickness of the film, δ. Measurements obtained varied between 40 and 300 μm (electronic supplementary material, figures S4 and S5). The technique used to measure δ is not very accurate. Nevertheless, since the influence of δ has been neglected at first order, the error made has no effect on our results.

(d) Estimation of the error on Δ

The impact point dispersal Δ corresponds to the standard deviation of the distribution of horizontal position of many drop impacts. We checked that the impact position follows a two-dimensional, Gaussian distribution (hypothesis test with a type I error of 5%). Due to the axisymmetry of the distribution and since samples are sufficiently large, taking only measurements along the x-axis is sufficient to estimate Δ. The error made on the measurement of Δ is estimated as follows, using a type I error of 1%: $N\Delta^2/\varsigma^2 \sim \chi^2(N-1)$, where N is the sample size and ς is the actual standard deviation of the entire population of drops impacting a stalagmite.

References

1. Baker A, Smith C, Jex C, Fairchild I, Genty D, Fuller L. 2008 Annually laminated speleothems: a review. *Int. J. Speleol.* **37**, 193–206. (doi:10.5038/1827-806x.37.3.4)

2. Baker A, Genty D, Dreybrodt W, Barnes WL, Mockler NJ, Grapes J. 1998 Testing theoretically predicted stalagmite growth rate with recent annually laminated samples: implications for past stalagmite deposition. *Geochim. Cosmochim. Acta* **62**, 393–404. (doi:10.1016/s0016-7037(97)00343-8)

3. Dreybrodt W. 1988 *Processes in karst systems. Physics, chemistry, and geology*. Berlin, Germany: Springer.

4. Baldini JUL. 2010 Cave atmosphere controls on stalagmite growth rate and palaeoclimate records. *J. Geol. Soc.* **336**, 283–294. (doi:10.1144/sp336.15)

5. Sherwin CM, Baldini JUL. 2011 Cave air and hydrological controls on prior calcite precipitation and stalagmite growth rates: implications for palaeoclimate reconstructions using speleothems. *Geochim. Cosmochim. Acta* **75**, 3915–3929. (doi:10.1016/S1251-8050(97)88288-2)

6. Dreybrodt W. 1999 Chemical kinetics, speleothem growth and climate. *Boreas* **28**, 347–356. (doi:10.1080/030094899422073)

7. Genty D. 1993 Mise en évidence d'alternances saisonnières dans la structure interne des stalagmites. Intérêt pour la reconstitution des paléoenvironnements continentaux. *C. R. Acad. Sci. Paris* **317**, 1229–1236. (doi:10.1016/S1251-8050(97)88288-2)

8. Genty D *et al.* 2014 Rainfall and cave water isotopic relationships in two South-France sites. *Geochim. Cosmochim. Acta* **131**, 323–343. (doi:10.1016/j.gca.2014.01.043)

9. Genty D, Deflandre G. 1998 Drip flow variations under a stalactite of the Père Noël cave (Belgium). Evidence of seasonal variations and air pressure constraints. *J. Hydrol.* **211**, 208–232. (doi:10.1016/s0022-1694(98)00235-2)

10. Mariethoz G, Baker A, Sivakumar B, Hartland A, Graham P. 2012 Chaos and irregularity in karst percolation. *Geophys. Res. Lett.* **39**. (doi:10.1029/2012gl054270)

11. Curl RL. 1973 Minimum diameter stalagmites. *J. Caves Karst Stud.* **35**, 1–9.

12. Baker A, Mattey D, Baldini JUL. 2014 Reconstructing modern stalagmite growth from cave monitoring, local meteorology, and experimental measurements of dripwater films. *Earth Planet Sci. Lett.* **392**, 239–249. (doi:10.1016/j.epsl.2014.02.036)

13. Short MB, Baygents JC, Beck JW, Stone DA, Toomey RS, Goldstein RE. 2005 Stalactite growth as a free-boundary problem: a geometric law and its platonic ideal. *Phys. Rev. Lett.* **94**, 018501. (doi:10.1103/physrevlett.94.018501)

14. Short MB, Baygents JC, Goldstein RE. 2005 Stalactite growth as a free-boundary problem. *Phys. Fluids* **17**, 083101. (doi:10.1063/1.2006027)

15. Genty D, Quinif Y. 1996 Annually laminated sequences in the internal structure of some Belgian stalagmites - importance for paleoclimatology. *J. Sediment. Res.* **66**, 275–288. (doi:10.1306/D426831A-2B26-11D7-8648000102C1865D)

16. Tan M, Baker A, Genty D, Smith C, Esper J, Cai B. 2006 Applications of stalagmite laminae to paleoclimate reconstructions: comparison with dendrochronology/climatology. *Quat. Sci. Rev.* **25**, 2103–2117. (doi:10.1016/j.quascirev.2006.01.034)

17. Labuhn I *et al.* 2015 A high-resolution fluid inclusion $\delta^{18}O$ record from a stalagmite in SW France: modern calibration and comparison with multiple proxies. *Quat. Sci. Rev.* **110**, 152–165. (doi:10.1016/j.quascirev.2014.12.021)

18. Burns S, Fleitmann D, Mudelsee M, Neff U, Matter A, Mangini A. 2002 A 780-year annually resolved record of Indian Ocean monsoon variation in a speleothem from south Oman. *J. Geophys. Res.* **107**, ACL 9-1–ACL 9-9. (doi:10.1029/2001jd001281)

19. Baker A, Asrat A, Fairchild IJ, Leng MJ, Wynn PM, Bryant C, Genty D, Umer M. 2007 Analysis of the climate signal contained within $\delta^{18}O$ and growth rate parameters in two Ethiopian stalagmites. *Geochim. Cosmochim. Acta* **71**, 2975–2988. (doi:10.1016/j.gca.2007.03.029)

20. Buhmann D, Dreybrodt W. 1985 The kinetics of calcite dissolution and precipitation in geologically relevant situations of karst areas: 1. Open system. *Chem. Geol.* **48**, 189–211. (doi:10.1016/0009-2541(85)90046-4)

21. Buhmann D, Dreybrodt W. 1985 The kinetics of calcite dissolution and precipitation in geologically relevant situations of karst areas: 2. Closed system. *Chem. Geol.* **53**, 109–124. (doi:10.1016/0009-2541(85)90024-5)

22. Genty D, Baker A, Vokal B. 2001 Intra- and inter-annual growth rate of modern stalagmites. *Chem. Geol.* **176**, 191–212. (doi:10.1016/s0009-2541(00)00399-5)

23. Sherwin CM, Baldini JUL. 2011 Cave air and hydrological controls on prior calcite precipitation and stalagmite growth rates: implications for palaeoclimate reconstructions using speleothems. *Geochim. Cosmochim. Acta* **75**, 3915–3929. (doi:10.1016/j.gca.2011.04.020)

24. Kaufmann G. 2003 Stalagmite growth and palaeo-climate: the numerical perspective. *Earth Planet. Sci. Lett.* **214**, 251–266. (doi:10.1016/s0012-821x(03)00369-8)

25. Romanov D, Kaufmann G, Dreybrodt W. 2008 Modeling stalagmite growth by first principles of chemistry and physics of calcite precipitation. *Geochim. Cosmochim. Acta* **72**, 423–437. (doi:10.1016/j.gca.2007.09.038)

26. Romanov D, Dreybrodt W. 2008 Regular stalagmites: the theory behind their shape. *Acta Carsol.* **37**, 175–184. (doi:10.3986/ac.v37i2-3.145)

27. Ambravaneswaran B, Phillips SD, Basaran OA. 2000 Theoretical analysis of a dripping faucet. *Phys. Rev. Lett.* **85**, 5332–5335. (doi:10.1103/physrevlett.85.5332)

28. Curl RL. 1972 Minimum diameter stalactites. *J. Caves Karst Stud.* **34**, 129–136.

29. Clanet C, Lasheras JC. 1999 Transition from dripping to jetting. *J. Fluid Mech.* **383**, 307–326. (doi:10.1017/s0022112098004066)

30. Bourges F, Genthon P, Mangin A, D'Hulst D. 2006 Microclimates of L'Aven d'Orgnac and other French limestone caves (Chauvet, Esparros, Marsoulas). *Int. J. Climatol.* **26**, 1651–1670. (doi:10.1002/joc.1327)

31. Duan Z, He B, Duan Y. 2015 Sphere drag and heat transfer. *Sci. Rep.* **5**. (doi:10.1038/srep12304)

32. Reyssat E. 2007 *Gouttes, films et jets: quand les écoulements modèlent les interfaces*. Paris, FR: Université Paris-Diderot - Paris VII. See https://tel.archives-ouvertes.fr/tel-00169432.

33. Ern P, Risso F, Fabre D, Magnaudet J. 2012 Wake-induced oscillatory paths of bodies freely rising or falling in fluids. *Annu. Rev. Fluid Mech.* **44**, 97–121. (doi:10.1146/annurev-fluid-120710-101250)

34. Bagchi P, Balachandar S. 2003 Effect of turbulence on the drag and lift of a particle. *Phys. Fluids* **15**, 3496–3513. (doi:10.1063/1.1616031)

35. Achenbach E. 1974 Vortex shedding from spheres. *J. Fluid Mech.* **62**, 209–221. (doi:10.1017/s0022112074000644)

36. Johnson TA, Patel VC. 1999 Flow past a sphere up to a Reynolds number of 300. *J. Fluid Mech.* **378**, 19–70. (doi:10.1017/s0022112098003206)

37. Bouchet G, Mebarek M, Dusek J. 2006 Hydrodynamic forces acting on a rigid fixed sphere in early transitional regimes. *Eur. J. Mech. B-Fluid* **25**, 321–336. (doi:10.1016/j.euromechflu.2005.10.001)

38. Ploumhans P, Winckelmans GS, Salmon JK, Leonard A, Warren MS. 2002 Vortex methods for direct numerical simulation of three-dimensional bluff body flows: application to the sphere at $Re = 300$, 500, and 1000. *J. Comput. Phys.* **178**, 427–463. (doi:10.1006/jcph.2002.7035)

39. Yun G, Kim D, Choi H. 2006 Vortical structures behind a sphere at subcritical Reynolds numbers. *Phys. Fluids* **18**, 015102. (doi:10.1063/1.2166454)

40. Jones DA, Clarke DB. 2008 *Simulation of flow past a sphere using the fluent code*. Australia: Maritime Platforms Division. DSTO Defence Science and Technology Organisation.

41. Rodriguez I, Borell R, Lehmkuhl O, Perez Segarra CD, Oliva A. 2011 Direct numerical simulation of the flow over a sphere at $Re = 3700$. *J. Fluid Mech.* **679**, 263–287. (doi:10.1017/jfm.2011.136)

42. Clanet C, Béguin C, Richard D, Quéré D. 2004 Maximal deformation of an impacting drop. *J. Fluid Mech.* **517**, 199–208. (doi:10.1017/s0022112004000904)

43. Yarin AL. 2006 Drop impact dynamics: splashing, spreading, receding, bouncing. *Annu. Rev. Fluid Mech.* **38**, 159–192. (doi:10.1146/annurev.fluid.38.050304.092144)

44. Wang AB, Chen CC. 2000 Splashing impact of a single drop onto very thin liquid films. *Phys. Fluids* **12**, 2155–2158. (doi:10.1063/1.1287511)

45. Gordillo J, Riboux G, Quintero ES. 2019 A theory on the spreading of impacting droplets. *J. Fluid Mech.* **866**, 159–192. (doi:10.1017/jfm.2019.117)

46. Lejeune S, Gilet T, Bourouiba L. 2018 Edge effect: liquid sheet and droplets formed by drop impact close to an edge. *Phys. Rev. Fluids* **3**, 083601. (doi:10.1103/physrevfluids.3.083601)

47. Laan N, de Bruin KG, Bartolo D, Josserand C, Bonn D. 2014 Maximum diameter of impacting liquid droplets. *Phys. Rev. Appl.* **2**, 044018. (doi:10.1103/PhysRevApplied.2.044018)